The crust and upper mantle discontinuity structure beneath Alaska inferred from receiver functions

Yinshuang Ai[a,b,*], Dapeng Zhao[b], Xing Gao[c], Weiwei Xu[a]

[a] *Institute of Geology and Geophysics, Chinese Academy of Sciences, Deshengmenwai, Qijiahuozi, Chaoyang District, Beijing 100029, China*
[b] *Geodynamics Research Center, Ehime University, Matsuyama 790-8577, Japan*
[c] *Institute of Tibetan Plateau Research, Chinese Academy of Sciences, Deshengmenwai, Qijiahuozi, Chaoyang District, Beijing 100029, China*

Abstract

In this study, three receiver function stacking methods are used to study the detailed crust and upper mantle structure beneath south-central Alaska. We used teleseismic waveform data recorded by 36 stations in the Broadband Experiment Across the Alaska Range (BEAAR) and 4 permanent stations in Alaska. $H - \kappa$ stacking method using P-to-S converted wave and its multiply reflected waves between the Earth's surface and the Moho discontinuity is adopted to estimate the crustal thickness (H) and average crustal V_P/V_S ratio (κ) in this region. The receiver function results for 24 stations show that the crustal thickness under Alaska ranges from 26.0 to 42.6 km with an average value of 33.8 km, and the V_P/V_S ratio varies from 1.66 to 1.94 with an average value of 1.81 which corresponds to an average Poisson's ratio of 0.277 with a range from 0.216 to 0.320. High Poisson's ratios under some stations are possibly caused by partial melting in the crust and the uppermost mantle. Common converted point (CCP) stacking results of receiver functions along three lines show clear Moho and slab images under this subduction zone. The depths of the slab from our CCP stacking images are consistent with those estimated from the Wadati–Benioff Zone (WBZ). In the area between two stations DH2 (147.8°W, 63.3°N) and DH3 (147.1°W, 63.0°N), a Moho depth offset of about 10 km is found by both the $H - \kappa$ and CCP stacking techniques. Common depth point (CDP) stacking of receiver functions shows not only the 410-, 520- and 660-km discontinuities, but also significant variations (−30 to 15 km) in the transition zone thickness under the southwest and southeast parts of the study region. The transition zone becomes thinner by 20–30 km, indicating that the temperature there is 150–200 K higher than that of the normal mantle.

* Corresponding author. Tel.: +86 10 62007354/81 89 927 8257; fax: +86 10 62010846/81 89 927 8167.
   E-mail addresses: ysai@mail.igcas.ac.cn, y-ai@sci.ehime-u.ac.jp (Y. Ai).

1. Introduction

Receiver function methods have been widely used to study the interior structure of the Earth since they were first introduced to seismology about three

decades ago (Langston, 1977; Vinnik, 1977). While early receiver function studies were mainly used to investigate the crustal structure (Owens et al., 1984; Ammon, 1991), more advanced receiver function stacking methods have been developed recently to study the crust and upper mantle discontinuity structures (e.g., Dueker and Sheehan, 1997; Yuan et al., 1997; Zhu and Kanamori, 2000), thanks to the increasing number of digital seismic stations and modern data processing methods from exploration seismology. These stacking methods have been widely used in many regions such as subduction zones (Yuan et al., 1997; Kind et al., 2002; Ai et al., 2003). These results have provided important new constraints on the composition and temperature of the crust and upper mantle as well as the interaction between the subducting slab and the mantle transition zone (Chevrot and van der Hilst, 2000; Simmons and Gurrola, 2000; Ferris et al., 2003).

Alaska is located in the northern Pacific subduction zone. The Pacific plate subducts northwestwards beneath south-central Alaska at a rate of about 54 mm/year (Brocher et al., 1994). Intermediate-depth earthquakes occur actively from 50 to about 150 km depth. Many geophysical studies of the crust and upper mantle structure have been carried out beneath Alaska. 3D regional P wave tomography revealed that the subducting Pacific slab has a thickness of about 50 km and a P wave velocity 3–6% higher than the surrounding mantle (Zhao et al., 1995). A receiver function study revealed a 11–22 km thick low velocity layer at the top of the slab, which may represent a thick serpentinized zone or a thick exotic terrane subducting along with the Pacific plate (Ferris et al., 2003). The previous receiver function study (Ferris et al., 2003) focused on only one transect along NW–SE direction in south-central Alaska and used only four teleseismic events that occurred in western Asia. In addition, the crustal Poisson's ratio, an important parameter for understanding the composition and evolution of the crust, was still poorly constrained beneath Alaska due to the lack of seismic data. Moreover, the depth and geometry of the 410 and 660 km discontinuities (hereafter we call them the 410 and the 660) have not been investigated yet for this region. Such information is very important for understanding the composition and thermal structure of the mantle transition zone.

In this study, we used a large amount of waveform data from teleseismic events recorded by stations in the Broadband Experiment Across the Alaska Range (BEAAR) and several permanent stations in Alaska, and used receiver functions stacking techniques to study the crustal and mantle structure beneath south-central Alaska in detail. First, we applied the $H - \kappa$ stacking scheme (Zhu and Kanamori, 2000) to the direct P-to-S phase and the later multiple phases from the Moho to determine the crustal thickness and V_P/V_S ratio under each station simultaneously. Second, we used the common converted point (CCP) stacking of receiver functions (Zhu, 2000, 2002) to constrain the crust and slab images beneath Alaska. In recent years, the common depth point (CDP) method (Dueker and Sheehan, 1997; Ai et al., 2003) has been widely used to study the 410- and 660-km discontinuities, which are interpreted to be phase transformations from α-olivine to β-spinel and from γ-spinel to perovskite and magnesiowustite, respectively (Ito and Takahashi, 1989). In this study, we sorted and stacked the receiver functions according to the CDP to study the upper mantle discontinuities as well as the transition zone beneath this region.

2. Data

We utilized two data sets in this study. Most of the data are from the portable BEAAR IRIS/PASSCAL network (Fig. 1). Among the 36 stations of this network, 7 stations were operating from 1999 to 2000, 36 stations were operating during June–September 2000, and 17 stations were continuously operating until August 2001 (Ferris et al., 2003). Data from all the portable stations were recorded continuously at 50 samples per second with either Güralp CMG3T or CMG3ESP sensors (Ferris et al., 2003). The remaining data are from four permanent stations, which are MCK from the Alaska Regional Network, IL31 from the International Miscellaneous Stations, COL and COLA (simplified as code COA in this paper) from the Global Seismograph Network (GSN). All of the portable and permanent stations were deployed in south-central Alaska where the subducting Pacific slab is at depths of 50–150 km. Teleseismic events in the distance range between 30° and 90° with magnitude greater than 5.8 for the portable stations, and with magnitude greater than 6.0 for the permanent stations, were selected. For the four per-
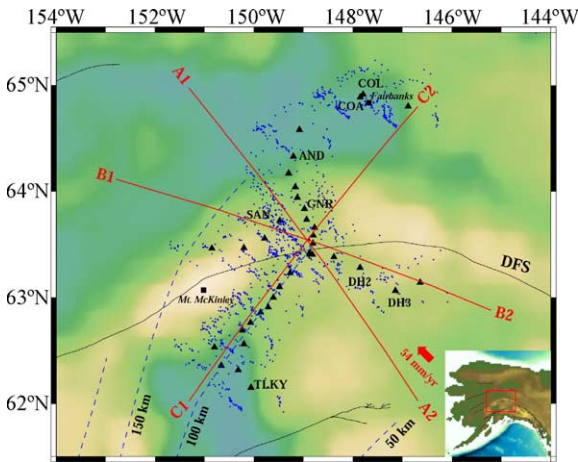
Fig. 1. Map showing the present study region in south-central Alaska (see also the insert map). Locations of broadband stations are shown by black triangles. The arrow shows the direction of the Pacific plate convergence. Dashed lines denote the depth contours of the subducting Pacific slab (after Gudmundsson and Sambridge, 1998). Dots represent the piercing points of converted S waves at depth of 120 km. The 1D *iasp91* velocity model with a modified crustal structure for the Alaska region was used to calculate the locations of the piercing points (after Kennett and Engdahl, 1991; Laske et al., 2001). The locations of three stacking lines are shown in A1–A2, B1–B2 and C1–C2. DFS denotes the Denali Fault System. Fault locations are modified after Hreinsdottir et al. (2003). Some station codes are shown near stations with three or four capital letters.
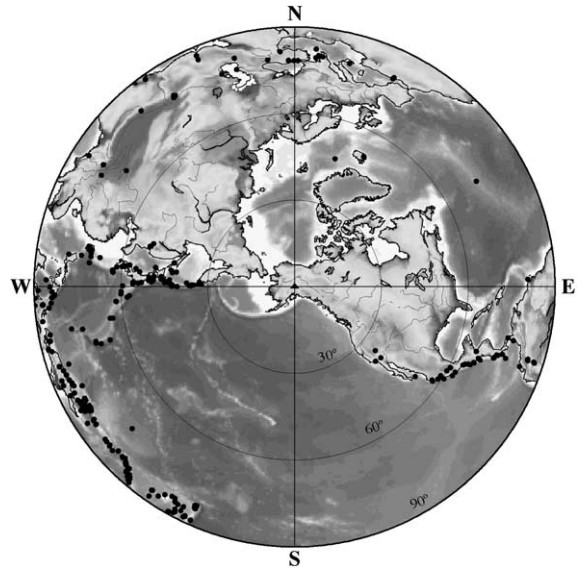
manent stations, we selected data recorded from June 2000 to December 2000 at MCK, from March 1991 to October 1997 at COL, from March 1998 to December 2002 at IL31, and from June 1996 to December 2002 at COA, respectively.

In the present study, observed seismograms were windowed from 20 s before to 100 s after the first P wave arrivals, then a 2.5 Hz Gaussian parameter, which excludes frequencies over about 1.2 Hz (Ammon, 1991), was used to isolate receiver functions by using the maximum entropy deconvolution method (Wu and Zeng, 1998; Ai et al., 2003). Data selection is a crucial point in receiver functions analysis, especially if the Poisson's ratio is to be determined from the joint analysis of Moho conversions and multiples (S. Chevrot, personal communication, 2004). In our study, we visually selected records with stable and high signal-to-noise ratios for each station to make sure that the P-to-S converted phase from Moho and its two later multiple phases are present. The number of receiver

Fig. 2. Epicenter distribution of teleseismic events used in this study. The map center (triangle) is (149.0°W, 63.5°N).

functions selected varies from 4 at station RNDN to 123 at station COA. In total, we obtained 1804 receiver functions for the 40 stations. In total, 1804 receiver functions were calculated from 302 teleseismic events. Most of the events are distributed on the west and southwest of the study region (Fig. 2).

3. Crustal thickness and Poisson's ratio

One of the most useful stacking methods in receiver function analysis is the $H - \kappa$ stacking to estimate the average thickness and Poisson's ratio of the crust (Zhu and Kanamori, 2000; Chevrot and van der Hilst, 2000). Given the crustal thickness H and average crustal velocities V_P and V_S, the delay times between P and P-to-S phases from the Moho and their multiple phases can be expressed by the following formulae (Zhu and Kanamori, 2000):

$$t_{Ps} = H \left(\sqrt{\frac{1}{V_S^2} - p^2} - \sqrt{\frac{1}{V_P^2} - p^2} \right) \tag{1}$$

$$t_{PpPs} = H \left(\sqrt{\frac{1}{V_S^2} - p^2} + \sqrt{\frac{1}{V_P^2} - p^2} \right) \tag{2}$$

$$t_{PpSs+PsPs} = 2H\sqrt{\frac{1}{V_S^2} - p^2} \quad (3)$$

where p is the ray parameter. Thus, the delay times depend on three crustal parameters: H, V_P and V_S. Since they are more sensitive to V_P/V_S ratio κ than to V_P, we fixed V_P as a known parameter. Then the delay times only depend on H and V_S. In this case, a straightforward $H-\kappa$ domain stacking is defined as (Zhu and Kanamori, 2000):

$$s(H, \kappa) = w_1 r(t_{Ps}) + w_2 r(t_{PpPs}) - w_3 r(t_{PpSs+PsPs}) \quad (4)$$

where $r(t)$ is the radial receiver function, w_i are weighting factors with $\sum w_i = 1$. In this way, by stacking receiver functions from events at different distances, the $s(H,\kappa)$ reaches a maximum when all the three phases are stacked coherently with the best estimation of H and κ. Using the lower-order Taylor expansion of $s(H,\kappa)$ at the maximum, we can get the variances of H and κ (Zhu and Kanamori, 2000):

$$\sigma_H^2 = \frac{2\sigma_s}{\partial^2 s/\partial H^2} \quad (5)$$

$$\sigma_\kappa^2 = \frac{2\sigma_s}{\partial^2 s/\partial \kappa^2} \quad (6)$$

where σ_s is the estimated variance of $s(H,\kappa)$ from stacking. Then we can estimate the Poisson's ratio σ from V_P/V_S ratio using the relation:

$$\sigma = \frac{1}{2}\left(1 - \left[\left(\frac{V_P}{V_S}\right)^2 - 1\right]^{-1}\right) \quad (7)$$

In this study, the receiver functions at each station were stacked by using Eq. (4) with $w_1 = 0.5$, $w_2 = 0.3$, $w_3 = 0.2$, respectively. These values were chosen to balance the weights for the P-to-S converted phase from Moho and its later multiple phases. We also used the different weights ($w_1 = 0.7$, $w_2 = 0.2$, $w_3 = 0.1$) to perform our $H-\kappa$ stacking, and found that the weights chosen in the previous ones were better. We chose an average crustal P velocity of 6.7 km/s based on the previous work in this region (Ferris et al., 2003). Crustal thickness H and V_P/V_S ratio are constrained to vary between 20 and 45 km and between 1.6 and 2.0, respectively.

Fig. 3 shows a selection of receiver functions recorded by station GNR. Stacking 32 receiver functions for this station gives a crustal thickness of 32.8 km with a crustal V_P/V_S ratio of 1.88 (Fig. 4c). The dashed lines correspond to the average travel time curves of the
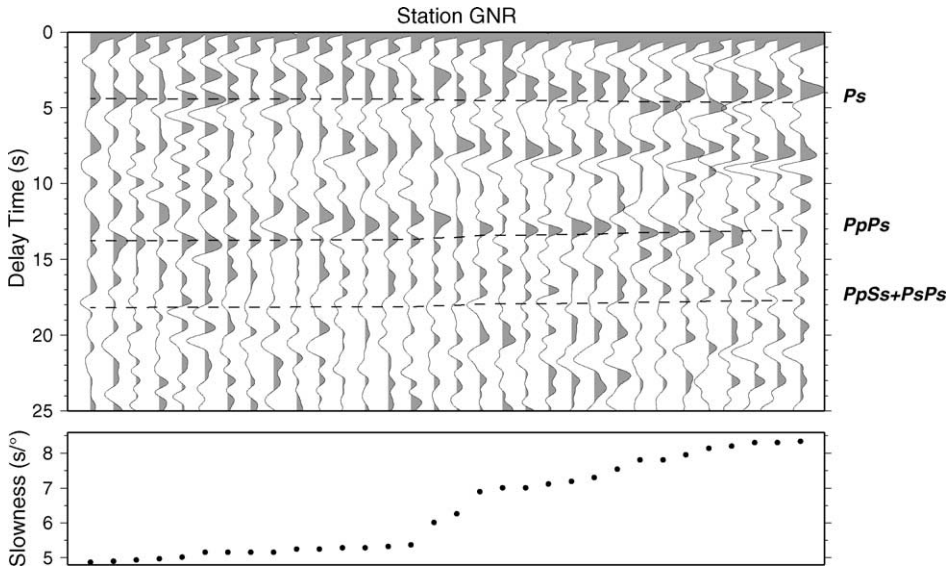

Fig. 3. Receiver function profile for station GNR, sorted according to slowness. The station location is shown in Fig. 1. The dashed lines show the predicted arrival times of Moho converted and multiply reflected waves using the crustal parameters that give the maximum amplitude of the stacks in Fig. 4c.
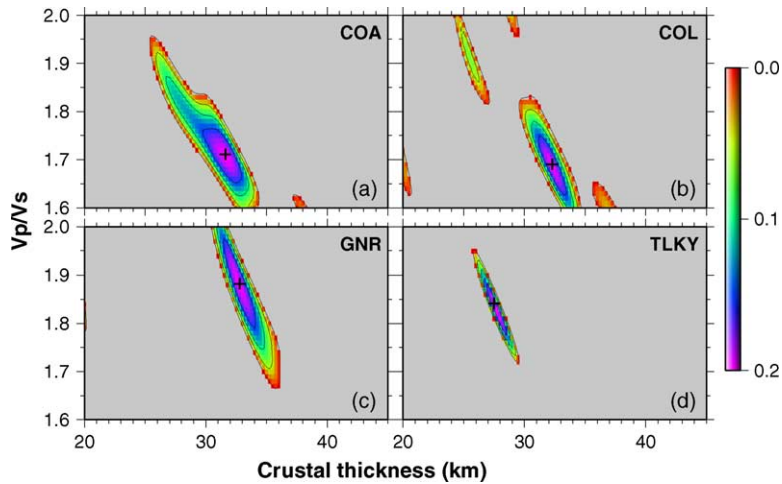
Fig. 4. $H - \kappa$ stacking results for V_P/V_S and crustal thickness under four seismic stations. The different colors (gray in print) show the different stacking values of $s(H,\kappa)$. The cross symbol denotes the maximum $s(H,\kappa)$ when the correct crustal thickness and V_P/V_S ratio are used in the stacking. The station codes are shown in the upper right corner. (For interpretation of the references to color in this figure legend, the reader is referred to the web version of this article.)

Moho converted and multiply reflected phases. These average curves are calculated by Eqs. (1)–(3) using a crustal thickness of 32.8 km and a crustal V_P/V_S of 1.88 shown in Fig. 4c. Some of the observed Moho converted and multiply reflected phases disaccord with the curves, which may reflect the lateral variations of the crustal thickness under this station.

As examples of the stacking results, we chose four stations to show the stacking amplitude images for different crustal thickness and V_P/V_S (Fig. 4). Station COA is a GSN station near Fairbanks. Different crustal thickness and V_P/V_S ratios lead to different stacking values of $s(H,\kappa)$. The maximum $s(H,\kappa)$ resulted from stacking 123 receiver functions leads to a crustal thickness of 31.6 km and a crustal V_P/V_S ratio of 1.71 (Poisson's ratio of 0.241) for this station (Fig. 4a). For station COL, not far away from station COA, The maximum $s(H,\kappa)$ resulted from stacking 14 receiver functions leads to a crustal thickness of 32.3 km with a crustal V_P/V_S ratio of 1.69 (Poisson's ratio 0.231) (Fig. 4b). Therefore, these two stations have a similar crustal thickness and lower Poisson's ratios around 0.24. However, for BEAAR network stations GNR and TLKY, stacking 32 and 118 receiver functions results in crustal thickness of 32.8 and 27.5 km and crustal V_P/V_S ratios of 1.88 and 1.84 (Poisson's ratios 0.303 and 0.291), respectively. These two stations have higher Poisson's ratios than that at stations COA and COL.

Due to the absence of a clear converted phase from the Moho or its later multiple phases, few data available, very complicated site responses, or multiple phases from shallower discontinuities at some of the stations, as shown in Table 1, crustal thickness and V_P/V_S were estimated only for 24 stations. $H - \kappa$ stack-
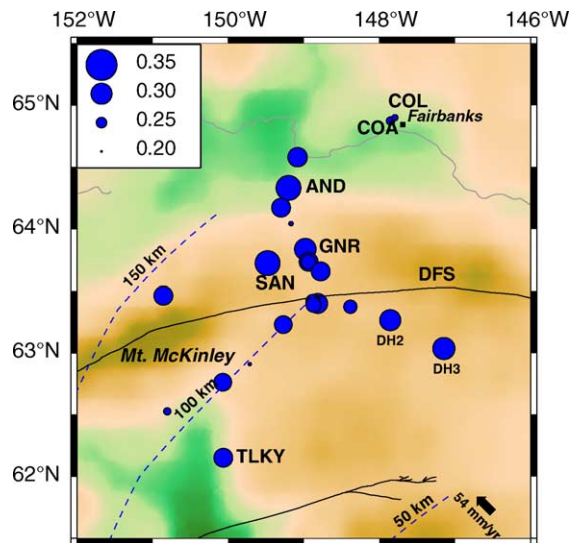

Fig. 5. The estimated Poisson's ratios for 24 seismic stations. Some station codes are shown near stations with three or four capital letters.

Table 1
Results of the receiver function analysis for 24 stations in Alaska

Station	Network	Longitude (°)	Latitude (°)	No. of traces	H (km)	V_P/V_S	σ
AND	BEAAR	−149.200	64.331	16	27.8 ± 1.3	1.94 ± 0.09	0.319
BSH	BEAAR	−149.295	64.171	7	31.0 ± 1.1	1.78 ± 0.06	0.269
COA	GSN	−147.851	64.874	123	31.6 ± 2.6	1.71 ± 0.10	0.241
COL	GSN	−147.793	64.900	14	32.3 ± 0.9	1.69 ± 0.05	0.231
DH1	BEAAR	−148.383	63.373	36	42.6 ± 1.6	1.77 ± 0.07	0.264
DH2	BEAAR	−147.855	63.265	12	39.8 ± 0.7	1.88 ± 0.04	0.302
DH3	BEAAR	−147.144	63.035	33	31.5 ± 1.5	1.89 ± 0.09	0.306
FID	BEAAR	−150.069	62.762	15	39.7 ± 1.1	1.83 ± 0.05	0.286
GNR	BEAAR	−148.978	63.834	32	32.8 ± 1.4	1.88 ± 0.10	0.303
GOO	BEAAR	−149.270	63.229	70	34.8 ± 0.8	1.82 ± 0.04	0.285
MCK	AK	−148.935	63.732	45	33.2 ± 0.8	1.84 ± 0.04	0.290
MCK	BEAAR	−148.937	63.732	34	34.0 ± 1.2	1.78 ± 0.07	0.269
NNA	BEAAR	−149.079	64.580	80	26.0 ± 1.4	1.85 ± 0.09	0.295
PVW	BEAAR	−150.804	62.528	25	33.8 ± 0.7	1.70 ± 0.04	0.236
PYY	BEAAR	−149.712	62.909	16	30.0 ± 0.8	1.66 ± 0.04	0.216
RCK	BEAAR	−149.166	64.041	48	32.6 ± 1.6	1.67 ± 0.07	0.222
RNDE	BEAAR	−148.815	63.400	19	39.4 ± 1.0	1.86 ± 0.04	0.296
RNDN	BEAAR	−148.878	63.416	4	40.3 ± 1.1	1.78 ± 0.05	0.270
RNDS	BEAAR	−148.868	63.390	14	40.1 ± 1.1	1.78 ± 0.05	0.271
SAN	BEAAR	−149.477	63.723	52	35.6 ± 1.0	1.94 ± 0.06	0.320
SOB	BEAAR	−149.299	64.170	16	30.0 ± 1.3	1.84 ± 0.08	0.290
TLKY	BEAAR	−150.061	62.150	118	27.5 ± 1.0	1.84 ± 0.06	0.291
WON	BEAAR	−150.854	63.462	31	29.3 ± 1.2	1.84 ± 0.08	0.291
YAN	BEAAR	−148.775	63.656	71	34.8 ± 1.4	1.84 ± 0.07	0.291

ing results at the 24 stations show that the crustal thickness ranges from 26.0 to 42.6 km with an average value of 33.8 km, and the V_P/V_S ratio varies from 1.66 to 1.94 with an average value of 1.81 which corresponds to the Poisson's ratio from 0.216 to 0.320 with an average value of 0.277. Fig. 5 shows the result of Poisson's ratio distribution in the study region.

4. Moho and slab images

To image the crustal structure of Alaska, we employed the CCP stacking method, which has become a popular seismological technique to study the crustal and upper mantle structure (Kosarev et al., 1999; Zhu, 2000, 2002). This method includes the following steps (Zhu, 2000, 2002): (1) the ray-path in depth domain of each receiver function is calculated by using a known background velocity model; (2) after correcting for the incidence angle effect, the amplitude at each point on the radial receiver function is assigned to its location on the ray-path where the P-to-S conversion occurred; (3) the studied profile is divided into certain size bins and all amplitudes in the same bin are stacked to obtain the average amplitude. In this way, we can obtain the crustal and upper mantle structure image along a certain profile.

We used the CCP stacking method to image the crustal and slab structure under Alaska. We selected three profiles, A1–A2 along NW–SE direction similar to that studied by Ferris et al. (2003), the other two transects B1–B2 and C1–C2 along W–E and SW–NE directions, respectively (Fig. 1). To suppress high-frequency noise in the receiver functions, a second-order zerophase Butterworth bandpass filter with corner frequencies 0.03–0.5 Hz was applied to all 1804 receiver functions. The 1D *iasp91* velocity model with a modified crustal structure for the Alaska region was used (Kennett and Engdahl, 1991; Laske et al., 2001). Since the stacking results are sensitive to the crustal V_P/V_S ratio, we used an average crustal V_P/V_S ratio of 1.81 which was obtained by using $H - \kappa$ stacking in this work. We used a bin size of 4 km along the profile and 0.5 km in depth. The width of the ray was calculated by considering its Fresnel zone to generate a smooth stacked image (Zhu, 2002).
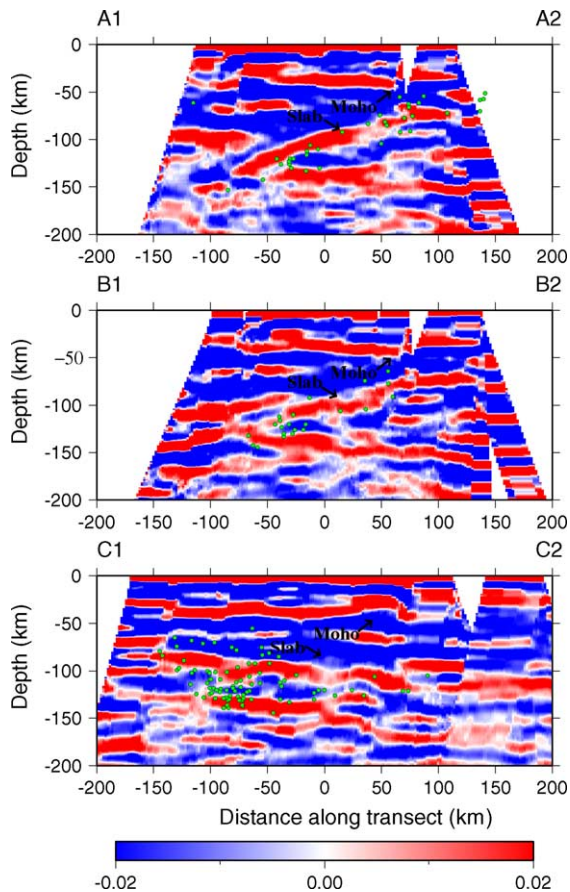
Fig. 6. CCP stacking of receiver functions for lines A1–A2, B1–B2 and C1–C2. The coordinate center location of three lines is at (149.0°W, 63.5°N). Red and blue colors denote the positive and negative stacking amplitude, respectively. Dots show earthquake hypocenters which occurred within a 50-km width of the stacking line and with depths between 50 and 150 km. (For interpretation of the references to color in this figure legend, the reader is referred to the web version of the article.)

The main results of our CCP stacking analyses are shown in Fig. 6. The trend of line A1–A2 is nearly parallel to the dip direction of the subducting Pacific slab (Fig. 1). Our CCP stacking results of this line show a 300-km-long coherent image of the upper mantle structure to a depth of 200 km. The Moho is visible as a strong conversion phase at depths of 30–50 km (Fig. 6). Compared with the west part of the profile, the Moho under the east part has a relative shallower depth. The most remarkable feature is a high amplitude converted phase at depths of 60–150 km from the east to the west,

which we interpret as a converted phase from the slab (Fig. 6). The depth of this phase is consistent with the location of WBZ and its amplitude turns to be weaker at depths greater than 150 km. A continuous negative amplitude phase, which represents a low velocity zone, exists at the top of the slab. The trend of line B1–B2 is almost oriented in the E–W direction, and the CCP stacking results of receiver functions show clear images of the Moho and the slab. The depth of the slab changes from 60 to 150 km from the east to the west, being consistent with the location of WBZ along this line. The line C1–C2 is nearly along the 100 km contour line of WBZ, however, the CCP stacking of receiver functions shows that the depth of slab changes from 80 to 120 km from the southwest to the northeast, and the Moho has a relative shallow depth under the northeastern part of this profile.

5. The upper mantle discontinuity and transition zone thickness variation

We used the CDP stacking of receiver functions to study the upper mantle discontinuities under Alaska. This method includes the following steps (Dueker and Sheehan, 1997; Ai and Zheng, 2003): (1) In order to calculate the delay time of the P-to-S converted phase relative to the direct P phase and the piercing point location of each P-to-S conversion at depths ranging from 0 to 800 km, ray-path in the depth domain of each receiver function is calculated by using a known background velocity model. (2) Since this delay time depends on both the epicentral distance and the depth of the P-to-S conversion, move-out corrections for the defined epicentral distance are carried out to all receiver functions. (3) Receiver functions within common depth point bins are geographically sorted and stacked along the defined stacking lines (Ai and Zheng, 2003).

In this study, a second-order zero phase Butterworth bandpass filter with corner frequencies of 0.03–0.2 Hz was applied to all the 1804 receiver functions. We used the same velocity model as we did in the CCP stacking of this study. The epicentral distance was defined at 67° when the move-out corrections were applied. At depths between 300 and 540 km and between 541 and 800 km, we stacked all the receiver functions whose piercing points at 410 and 660 km are within the same
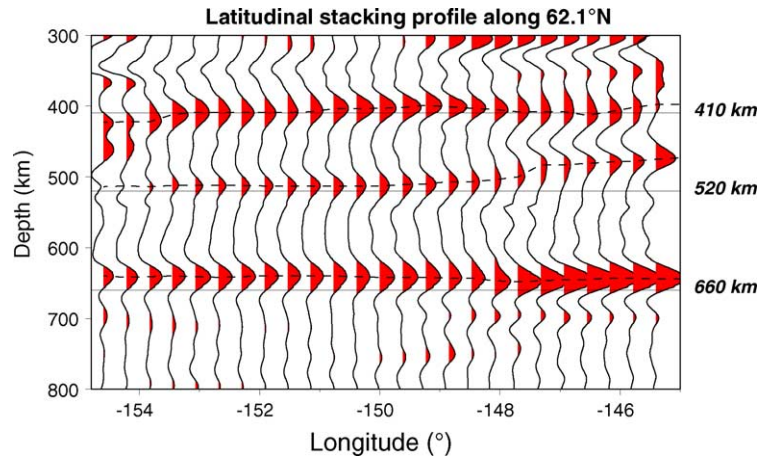
Fig. 7. The common depth point (CDP) stacking of receiver function profile along latitude 62.1°N. Positive polarity energy is plotted in red (gray in print) color. The observed depths of discontinuities are denoted with dashed lines. In the depth ranges of 300–540 and 541–800 km, all the receiver functions with piercing points at 410 and 660 km within the same bin are stacked, respectively. (For interpretation of the references to color in this figure legend, the reader is referred to the web version of this article.)

bin, respectively. In this case, we chose a circular bin size with a radius of 120 km.

A latitudinal CDP stacking profile is illustrated in Fig. 7. In this profile, more than 60 traces could be stacked in each bin, resulting in a clear upper mantle discontinuity image. The depth of the 410 (maximum amplitude part of converted phase shown in Fig. 7 with a dashed line) is consistent with the global average result (i.e., 410 km). However, the depth of the 660 is shallower. From longitudes 154.0 to 146.0°W, the depth of the 660 ranges from 640 to 650 km. We also see a clear image of the 520 km discontinuity, which is interpreted to be phase transformation from β-spinel to γ-spinel of olivine (Shearer, 1990). The depth of the 520 is about 510 km between 154.0 and 148.0°W, and is about 490 km to the east of 148.0°W. Compared with the other two discontinuities, the 520 has a weaker amplitude under the whole profile.

In our study, we converted receiver functions from the time domain to the depth domain using the 1D *iasp91* velocity model with a modified crustal structure for the Alaska region. This simple 1D velocity model may not be accurate enough for south-central Alaska where the Pacific slab is subducting and lateral velocity heterogeneities exist in the crust and upper mantle wedge. Therefore, the absolute depths of the upper mantle discontinuities should be considered with cautions. However, it is considered that strong ve-

locity heterogeneity mainly exists in the upper mantle down to about 410 km depth, and the mantle transition zone is less heterogeneous (Bostock, 1996; Vinnik et al., 1996). This is particularly true under Alaska as revealed by a recent global tomography (Zhao, 2004). Therefore in this work we focus on the thickness of the mantle transition zone (TZT) under Alaska instead of lateral velocity variations in the upper mantle.

To illustrate the TZT variation, we picked up the depths corresponding to the maximum positive amplitude of the 410 and the 660 in each bin. The TZT was determined by subtracting the depth of the 660 from that of the 410 for each bin in the study region. In the calculation we only selected bins with over 60 receiver functions within the same bin for the analysis. As shown in Fig. 8, the change in TZT varies considerably from −30 to 15 km under the study area. Under the south part of the central Denali fault system, the TZT is thinner than the average TZT (250 km) by about 20 km. In particular, under the southwest and southeast parts of Alaska, the TZT is 20–30 km thinner. Beneath the north part of the central Denali fault, the TZT anomaly varies from −10 to 10 km.

To assess the error in the depths of the upper mantle discontinuities and TZT, we performed a number of tests with different filtering parameters and different bin radii compared with our previous CDP stacking. We chose two second-order zero phase Butterworth
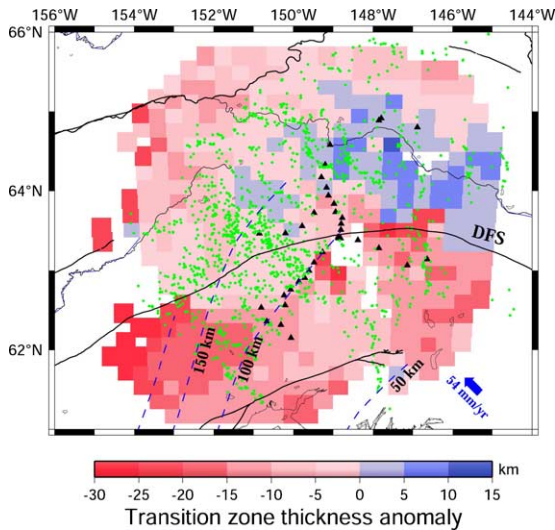
Fig. 8. Distribution of the transition zone thickness (TZT) anomaly under south-central Alaska. The values of the anomaly are relative to an average TZT of 250 km. Locations of broadband stations are shown by black triangles. Green dots represent piercing points of S waves at depth of 410 km. Dashed lines denote the depth contours of the subducting Pacific slab (after Gudmundsson and Sambridge, 1998). DFS denotes the Denali Fault System. (For interpretation of the references to color in this figure legend, the reader is referred to the web version of the article.)

bandpass filters with corner frequencies 0.03–0.3, 0.03–0.5 Hz to all of the 1804 receiver functions, respectively. These tests show that although the depths of the upper mantle discontinuities change within ±10 km, the TZT remains almost unchanged. For a higher bandpass filter (i.e., 0.03–0.5 Hz), the CDP stacking results in noisy images for the upper mantle discontinuities. We also chose different bin radii to test our CDP stacking. Larger bins contain more receiver functions in each bin, however, which results in larger spatial averaging. These tests also show that the depths of the upper mantle discontinuities change within ±10 km in most cases, but the TZT change is very small (less than 5 km). All the tests show that the 20–30 km thinning of the TZT under the southwest and southeast parts of Alaska is a robust feature.

6. Discussion

We found large variations in both the crustal thickness and Poisson's ratio in south-central Alaska. Stud-
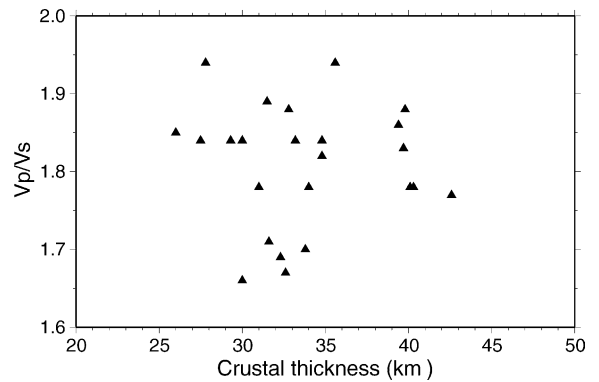

Fig. 9. V_P/V_S ratio vs. crustal thickness for 24 stations. No correlation is visible between them.

ies for other regions such as the Australian and the former Soviet Union demonstrated that there was a correlation (or anticorrelation) between the crustal thickness and Poisson's ratio (or V_P/V_S), i.e., a positive correlation exists for the Proterozoic crust while an anticorrelation exists for the Phanerozoic crust (Chevrot and van der Hilst, 2000; Egorkin, 1998). However, there seems no correlation between the crustal thickness and Poisson's ratio or V_P/V_S in south-central Alaska (Fig. 9). This discrepancy may be attributed to the following factors: (1) we obtained results from only 24 stations, which may be insufficient to reveal the correlation between the crustal thickness and Poisson's ratio; (2) many factors can cause variations in Poisson's ratio (Christensen, 1996); (3) the present study area is a complex subduction zone.

The average Poisson's ratio in the study region is 0.277, however, there are several stations with the Poisson's ratio values greater than 0.30, such as AND, DH2, DH3, GNR and SAN (Table 1). Petrologic experiments showed that changes in crustal compositions can cause variations in Poisson's ratio (Christensen, 1996). There is no simple correlation between Poisson's ratio and felsic and mafic rock compositions, however, an anticorrelation between the Poisson's ratio and SiO_2 content is found for rock with 55–75 wt.% SiO_2 (Christensen, 1996). A Poisson's ratio larger than 0.30 is rare in crustal rocks, except for serpentinite which can be as high as 0.35 (Chevrot and van der Hilst, 2000). Crustal melting has an important effect on the V_P/V_S ratio which increase with an increasing fluid fraction (Chevrot and van der Hilst, 2000). In Alaska,

there are many active volcanoes along the volcanic front. High Poisson's ratios under some stations may be due to melting in the crust and upper mantle wedge.

Our results from CCP stacking of receiver functions show clear subducting slab images in Alaska (Fig. 6). The CCP stacking results of receiver functions for line A1–A2 are consistent with the previous receiver function study in the same region (Ferris et al., 2003). Both results in this NW–SE direction stacking line show a clear slab image with a low velocity zone (negative phase in Fig. 6) at the top of the slab down to about 150 km depth. However, our results in line A1–A2 show a better image since many more receiver functions are used. For stacking lines B1–B2 and C1–C2, which were not shown in the previous study (Ferris et al., 2003), the slab also shows up clearly. Along line B1–B2, a continuous slab image with a low velocity zone at the top of the slab is also visible down to a depth of 150 km. The slab depth in lines A1–A2 and B1–B2 is also consistent with the depth of WBZ in this region.

We also obtained clear Moho images from CCP stacking results of receiver functions (Fig. 6). Compared with the west part of the study region, the east part of study region has a relatively shallower Moho. From 60 km to the east in lines A1–A2 and B1–B2, we can see rapid variations in the Moho depth. In this narrow band of region, about 10 km Moho offset exists. To confirm this hypothesis, we chose two nearby stations DH2 and DH3 (Fig. 1) which are located at (147.855°W, 63.265°N) and (147.144°W, 63.035°N), respectively. Fig. 10 shows a receiver functions profile with back azimuths from 282° to 240° in station DH2 and from 282° to 224° in station DH3. The strongest P-to-S converted phases from the Moho are concentrated at about 5.5 s in station DH2, however, concentrated at about 4.3 s in station DH3. This 1.2 s delay time also imply that a large Moho offset exists within a narrow zone. $H - \kappa$ stacking of receiver functions also shows that the crustal thicknesses under stations DH2 and DH3 are 39.8 and 31.5 km, respectively, which is an another piece of evidence for the existence of the Moho offset.

Compared with the previous result using SS precursors (Shearer et al., 1999), the image of the upper mantle discontinuities beneath Alaska derived from receiver function stackings is more reliable. We see clear discontinuity phases of the 410, 520 and 660 (Fig. 7), which have 10–20 km undulations compared
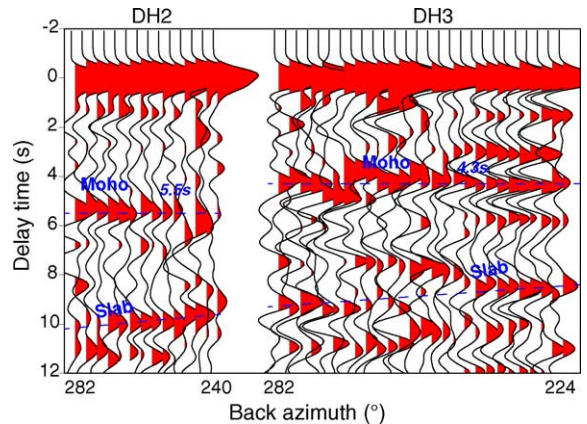

Fig. 10. A receiver functions profile with back azimuth from 282° to 240° in station DH2 and from 282° to 224° in station DH3. Dashed lines (observed phases) around 5.5 s under station DH2 and 4.3 s under station DH3 denote the P-to-S converted phases from Moho. Slab images are also marked by dashed lines.

with the global average. The upper mantle discontinuity structure from the global SS stacking, which uses long-period SS precursors from underside reflections off upper mantle discontinuities, usually has a lateral resolution of about 1000 km (Flanagan and Shearer, 1998; Gu and Dziewonski, 2002; Shearer et al., 1999). Thus, the detailed upper mantle discontinuity structure in a small region like the south-central Alaska is hard to reveal by using SS precursors. Lateral resolution provided by the receiver functions stacking techniques using converted phases at the upper mantle discontinuities is many times higher than that of SS precursors. One remarkable result of our study is that the 520 is well imaged under Alaska (Fig. 7), which was seldom detected purely by receiver function stackings.

Variations in the TZT can provide a more detailed "mantle thermometer" than the absolute depths of the 410 and 660 (Owens et al., 2000). If we use Clapeyron slops of +2.9 and −1.9 MPa/K for the 410 and 660 phase transformations, respectively (Bina and Helffrich, 1994), we can estimate the temperature variations in the TZT. In southwest and southeast parts (south of the Denali Fault System) of Alaska, a 20–30 km thinning of the transition zone corresponds to 150–200 K higher temperature than that of the normal mantle. However, in the north of the Denali Fault system, the temperature in the transition zone shows little difference from that of the normal mantle.

7. Conclusions

$H - \kappa$ stacking results for the receiver functions at 24 stations show that the crustal thickness under south-central Alaska ranges from 26.0 to 42.6 km with an average value of 33.8 km, and Poisson's ratio from 0.216 to 0.320 with an average value of 0.277. Partial melting in the crust and uppermost mantle is one possible cause for high Poisson's ratios (greater than 0.30) under some stations. CCP stacking results of receiver functions clearly show the Moho and slab under this subduction zone. Slab depths are consistent with those estimated from the Wadati–Benioff Zone. Between two stations DH2 (147.8°W, 63.3°N) and DH3 (147.1°W, 63.0°N), we found a 10-km offset in the Moho using both $H - \kappa$ and CCP methods. CDP stacking results of receiver functions show the 410, 520 and 660 discontinuities clearly. In the southwest and southeast parts of the study region, the mantle transition zone is 20–30 km thinner, which corresponds to 150–200 K higher temperature than that of the normal mantle.

Acknowledgments

References

Ai, Y., Zheng, T., 2003. The upper mantle discontinuity structure beneath eastern China. Geophys. Res. Lett. 30, 2089, doi:10.1029/2003GL017678.

Ai, Y., Zheng, T., Xu, W., He, Y., Dong, D., 2003. A complex 660 km discontinuity beneath northeast China. Earth Planet. Sci. Lett. 212, 63–71.

Ammon, C.J., 1991. The isolation of receiver function effects from teleseismic P waveforms. Bull. Seismol. Soc. Am. 81, 2504–2510.

Bina, C.R., Helffrich, G.R., 1994. Phase transition Clapeyron slops and transition zone seismic discontinuity topography. J. Geophys. Res. 99, 15853–15860.

Bostock, M.G., 1996. Ps conversions from the upper mantle transition zone beneath the Canadian landmass. J. Geophys. Res. 101, 8393–8402.

Brocher, T.M., Fuis, G.S., Fisher, M.A., Plafker, G., Moses, M.J., Taber, J.J., Christensen, N.I., 1994. Mapping the megathrust beneath the northern Gulf of Alaska using wide-angle seismic data. J. Geophys. Res. 99, 11663–11685.

Chevrot, S., van der Hilst, R.D., 2000. The Poisson ratio of the Australian crust: geological and geophysical implications. Earth Planet. Sci. Lett. 183, 121–132.

Christensen, N.I., 1996. Poisson's ratio and crustal seismology. J. Geophys. Res. 101, 3139–3156.

Dueker, K.G., Sheehan, A.F., 1997. Mantle discontinuity structure from midpoint stacks of converted P to S waves across the Yellowstone hotspot track. J. Geophys. Res. 102, 8313–8327.

Egorkin, A.V., 1998. Velocity structure, composition and discrimination of crustal provinces in the former Soviet Union. Tectonophysics 298, 395–404.

Ferris, A., Abers, G.A., Christensen, D.H., Veenstra, E., 2003. High resolution image of the subducted Pacific (?) plate beneath central Alaska, 50–150 km depth. Earth Planet. Sci. Lett. 214, 575–588.

Flanagan, M.P., Shearer, P.M., 1998. Global mapping of topography on transition velocity discontinuities by stacking SS precursors. J. Geophys. Res. 103, 2673–2692.

Gu, Y.J., Dziewonski, A.M., 2002. Global variability of transition zone thickness. J. Geophys. Res. 107, doi:10.1029/2001JB000489.

Gudmundsson, O., Sambridge, M., 1998. A regionalized upper mantle (RUM) seismic model. J. Geophys. Res. 103, 7121–7136.

Hreinsdottir, S., Freymueller, J.T., Fletcher, H.J., Larsen, C.F., Burgmann, R., 2003. Coseismic slip distribution of the 2002 M_W 7.9 Denali fault earthquake, Alaska, determined from GPS measurements. Geophys. Res. Lett. 30, 1670, doi:10.1029/2003GL017447.

Ito, E., Takahashi, E., 1989. Postspinel transformations in the system Mg_2SiO_4–Fe_2SiO_4 and some geophysical implications. J. Geophys. Res. 94, 10637–10646.

Kennett, B.L.N., Engdahl, E.R., 1991. Traveltimes for global earthquake location and phase identification. Geophys. J. Int. 105, 429–465.

Kind, R., Yuan, X., Saul, J., Nelson, D., Sobolev, S.V., Mechie, J., Zhao, W., Kosarev, G., Ni, J., Achauer, U., Jiang, M., 2002. Seismic images of crust and upper mantle beneath Tibet: evidence for Eurasian plate subduction. Science 298, 1219–1221.

Kosarev, G., Kind, R., Sobolev, S.V., Yuan, X., Hanka, W., Oreshin, W., 1999. Seismic evidence for a detached Indian lithospheric mantle beneath Tibet. Science 283, 1306–1309.

Langston, C.A., 1977. The effect of planar dipping structure on source and receiver responses for constant ray parameter. Bull. Seismol. Soc. Am. 67, 1029–1050.

Laske, G., Masters, G., Reif, C., 2001. CRUST 2.0: A New Global Crustal Model at 2 × 2 Degrees. http://mahi.ucsd.edu/Gabi/rem.html (last accessed March 2004).

Owens, T.J., Nyblade, A.A., Gurrola, H., Langston, C.A., 2000. Mantle transition zone structure beneath Tanzania. Geophys. Res. Lett. 27, 827–830.

Owens, T.J., Zandt, G., Taylor, S.R., 1984. Seismic evidence for an ancient rift beneath the Cumberland Plateau, Tennessee: a detailed analysis of broadband teleseismic P waveforms. J. Geophys. Res. 89, 7783–7795.

Shearer, P.M., 1990. Seismic imaging of upper mantle structure with new evidence for a 520-km discontinuity. Nature 344, 121–126.

Shearer, P.M., Flanagan, M.P., Hedlin, M.A.H., 1999. Experiments in migration processing of SS precursor data to image upper mantle discontinuity structure. J. Geophys. Res. 104, 7229–7242.

Simmons, N.A., Gurrola, H., 2000. Multiple seismic discontinuities near the base of the transition zone in the Earth's mantle. Nature 405, 559–562.

Vinnik, L.P., 1977. Detection of waves converted from P to SV in the mantle. Phys. Earth Planet. Inter. 15, 39–45.

Vinnik, L.P., Kosarev, G., Petersen, N., 1996. Mantle transition zone beneath Eurasia. Geophys. Res. Lett. 23, 1485–1488.

Wessel, P., Smith, W.H.F., 1995. New version of the Generic Mapping Tools (GMT) version 3.0 released. Eos Trans. AGU 76, 329.

Wu, Q., Zeng, R., 1998. The crustal structure of Qinghai-Xizang plateau inferred from broadband teleseismic waveform. Chinese J. Geophys. 41, 669–679 (in Chinese).

Yuan, X., Ni, J., Kind, R., Mechie, J., Sandvol, E., 1997. Lithospheric and upper mantle structure of southern Tibet from a seismological passive source experiment. J. Geophys. Res. 102, 27491–27500.

Zhao, D., 2004. Global tomographic images of mantle plumes and subducting slabs: insight into deep Earth dynamics. Phys. Earth Planet. Inter. 146, 3–34.

Zhao, D., Christensen, D., Pulpan, H., 1995. Tomographic imaging of the Alaska subduction zone. J. Geophys. Res. 100, 6487–6504.

Zhu, L., 2000. Crustal structure across the San Andreas Fault, Southern California from teleseismic converted waves. Earth Planet. Sci. Lett. 179, 183–190.

Zhu, L., 2002. Deformation in the lower crust and downward extent of the San Andreas Fault as revealed by teleseismic waveforms. Earth Planets Space 54, 1005–1010.

Zhu, L., Kanamori, H., 2000. Moho depth variation in southern California from teleseismic receiver functions. J. Geophys. Res. 105, 2969–2980.